Nanoscale Research Letters
a SpringerOpen Journal

NANO EXPRESS   **Open Access**

MnO$_2$ prepared by hydrothermal method and electrochemical performance as anode for lithium-ion battery

Lili Feng[1,2*], Zhewen Xuan[1,2], Hongbo Zhao[1,2], Yang Bai[1,2], Junming Guo[1,2], Chang-wei Su[1,2] and Xiaokai Chen[3*]

Abstract

Two α-MnO$_2$ crystals with caddice-clew-like and urchin-like morphologies are prepared by the hydrothermal method, and their structure and electrochemical performance are characterized by scanning electron microscope (SEM), X-ray diffraction (XRD), galvanostatic cell cycling, cyclic voltammetry, and electrochemical impedance spectroscopy (EIS). The morphology of the MnO$_2$ prepared under acidic condition is urchin-like, while the one prepared under neutral condition is caddice-clew-like. The identical crystalline phase of MnO$_2$ crystals is essential to evaluate the relationship between electrochemical performances and morphologies for lithium-ion battery application. In this study, urchin-like α-MnO$_2$ crystals with compact structure have better electrochemical performance due to the higher specific capacity and lower impedance. We find that the relationship between electrochemical performance and morphology is different when MnO$_2$ material used as electrochemical supercapacitor or as anode of lithium-ion battery. For lithium-ion battery application, urchin-like MnO$_2$ material has better electrochemical performance.

Keywords: Lithium-ion battery; Manganese dioxide; Hydrothermal method; Anode materials

Background

Manganese dioxides with diverse crystal morphologies are attracting a lot of attention because of their physical and chemical properties and wide applications in catalysis [1], biosensors [2], water treatment [3,4], electrochemical supercapacitors [5-9], and so on. Up to now, various MnO$_2$ crystals with different morphologies such as nanosphere [10,11], nanorod [12,13], nanowire [13], nanoflower [13,14], nanotube [15], pillow-shape [4], urchin-like [10,16], hollow nanosphere, hollow nanocube [3], and hollow cone [17] have been synthesized. MnO$_2$ crystals were already used in water treatment, gas sensors, electrochemical supercapacitors, and so on. For example, hollow spherical and cubic MnO$_2$ nanostructures prepared by Kirkendall effect showed good ability to remove organic pollutants in waste water [3]. Cao et al. had prepared pillow-shaped MnO$_2$ crystals which could remove about 85% of the Cd^{2+} in waste water [4]. Zhang et al. had prepared MnO$_2$ hollow nanospheres and nanowires used for ammonia gas sensor [2]. MnO$_2$ hollow nanospheres were found to exhibit enhanced sensing performance to ammonia gas at room temperature compared with MnO$_2$ nanowires. Ma et al. had prepared urchin-shaped MnO$_2$ and clew-like-shaped MnO$_2$ used for electrochemical supercapacitors [6]. They found the electrochemical performances differed with various morphologies, and clew-like MnO$_2$ nanospheres had higher capacitance and lower charge-transfer resistance due to their incompact structure. However, the application researches of MnO$_2$ as anode for lithium-ion battery were relatively few.

MnO$_2$ nanomaterials are recognized as anode materials since three-dimensional (3d) transition metal oxides (MO, where M is Fe, Co, Ni, and Cu) were proposed to serve as high theoretic capacity anodes for lithium-ion battery by Poizot et al. [18]. Before that, MnO$_2$ nanomaterials were usually used to prepare LiMn$_2$O$_4$ crystals as cathode for lithium-ion battery [19,20]. Chen's research group has made great contributions on the research of anode for lithium-ion battery [21,22]. Nevertheless, compared to the

* Correspondence: lilylian2003@163.com; xkchen@msn.com
[1]Engineering Research Center of Biopolymer Functional Materials of Yunnan, Yunnan Minzu University, Kunming 650500, China
[2]Key Laboratory of Chemistry in Ethnic Medicinal Resources, State Ethnic Affairs Commission & Ministry of Education, Yunnan Minzu University, Kunming 650500, China
Full list of author information is available at the end of the article

Springer

intensive investigation on Fe_2O_3, Fe_3O_4, SnO_2, CoO, and so on [23-28], the application investigation of MnO_2 nanomaterials on anodes for lithium-ion battery is still immature, although the investigations on their preparation are plentiful.

The research on MnO_2 anode is relatively complex because MnO_2 exists in several crystallographic forms such as α-, β-, γ-, and δ-type. For example, Zhao et al. [22] reported γ-MnO_2 crystals with hollow interior had high discharge capacity as 602.1 mAh g^{-1} after 20 cycles. Li et al. [15] found α-MnO_2 with nanotube morphology exhibited high reversible capacity of 512 mAh g^{-1} at a high current density of 800 mA g^{-1} after 300 cycles. Thus, from the above two examples, we could summarize that the electrochemical performance of MnO_2 crystals has relationship both with the crystallographic forms and with the morphologies. Therefore, the researches on the relationship of electrochemical performance with the morphologies and the relationship of electrochemical performance with the crystallographic forms are very essential.

In the present work, to enrich the relationship between electrochemical performances and morphologies, two α-MnO_2 crystals with caddice-clew-like and urchin-like morphologies were prepared by hydrothermal method. For lithium-ion battery application, urchin-like α-MnO_2 crystal with compact structure was found to have better electrochemical performance.

Methods
Synthesis and characterization of MnO_2 micromaterials prepared by hydrothermal method
All reagents purchased from the Shanghai Chemical Company (Shanghai, China) were of analytical grade and used without further purification. The MnO_2 micromaterials were prepared using the similar method described by Yu et al. [6] with some modifications. To prepare caddice-clew-like MnO_2 micromaterial, 1.70 g $MnSO_4 \cdot$ H_2O was dissolved in 15-mL distilled water with vigorous stirring. When the solution was clear, 20-mL aqueous solution containing 2.72 g $K_2S_2O_8$ was added to the above solution under continuous stirring. Then, the resulting transparent solution was transferred into a Teflon-lined stainless steel autoclave (50 mL) of 80% capacity of the total volume. The autoclave was sealed and maintained at 110°C for 6 h. After the reaction was completed, the autoclave was allowed to cool to room temperature naturally. The solid black precipitate was filtered, washed several times with distilled water to remove impurities, and then dried at 80°C in air for 3 h. The obtained caddice-clew-like MnO_2 micromaterial was collected for the following characterization.

Urchin-like MnO_2 micromaterial was prepared by the similar method, while after adding 1.70 g $MnSO_4 \cdot H_2O$

and 2.72 g $K_2S_2O_8$ into 35-mL distilled water, 2 mL H_2SO_4 was then added. Subsequently, the solution was transferred into a Teflon-lined stainless steel autoclave (50 mL), and the autoclave was sealed and maintained at 110°C for 6 h as well. After the reaction was completed, the autoclave was allowed to cool to room temperature naturally. The solid black precipitate was filtered, washed several times with distilled water to remove impurities, and then dried at 80°C in air for 3 h.

The crystallographic structures of the products were determined with X-ray diffraction (XRD) which were recorded on a Rigaku D/max-2200/PC (Rigaku, Beijing, China) with Cu target at a scanning rate of 7°/min with 2θ ranging from 10° to 70°. The morphological investigations of scanning electron microscope (SEM) images were taken on a field emission scanning electron microscope (FESEM; Zeiss Ultra, Oberkochen, Germany).

Electrochemical studies of MnO_2 micromaterials
Electrochemical performances of the samples were measured using CR2025 coin-type cells assembled in a dry argon-filled glove box. To fabricate the working electrode, a slurry consisting of 60 wt.% active materials, 10 wt.% acetylene black, and 30 wt.% polyvinylidene fluoride (PVDF) dissolved in *N*-methyl pyrrolidinone was casted on a copper foil and dried at 80°C under vacuum for 5 h. Lithium sheet was served as counter and reference electrode, while a Celgard 2320 membrane (Shenzhen, China) was employed as a separator. The electrolyte was a solution of 1 M $LiPF_6$ in ethylene carbonate (EC)-1,2-dimethyl carbonate (DMC) (1:1 in volume). Galvanostatical charge-discharge experiments were performed by Land electric test system CT2001A (Wuhan LAND Electronics Co., Ltd., Wuhan, China) at a current density of 0.2 C between 0.01 and 3.60 V (versus Li/Li$^+$). Cyclic voltammogram (CV) tests were carried out on an electrochemical workstation (CHI604D, Chenhua, Shanghai, China) from 0.01 to 3.60 V (versus Li/Li$^+$). Electrochemical impedance spectroscopy (EIS) measurements were performed on an electrochemical workstation (CHI604D, Chenhua, Shanghai, China), and the frequency ranged from 0.1 Hz to 100 kHz with an applied alternating current (AC) signal amplitude of 5 mV.

Results and discussion
Structure and morphology
The SEM images of the MnO_2 micromaterials are displayed in Figure 1. The SEM study in Figure 1a indicates that the MnO_2 prepared under the neutral reaction conditions is a nanowire 55 to 83 nm in diameter and several micrometers in length for average. Moreover, these nanowires aggregate into spherical shape with diameter of about 2 to 4 μm, and the MnO_2 micromaterials are like a caddice clew. To mention the sample easily, we call this
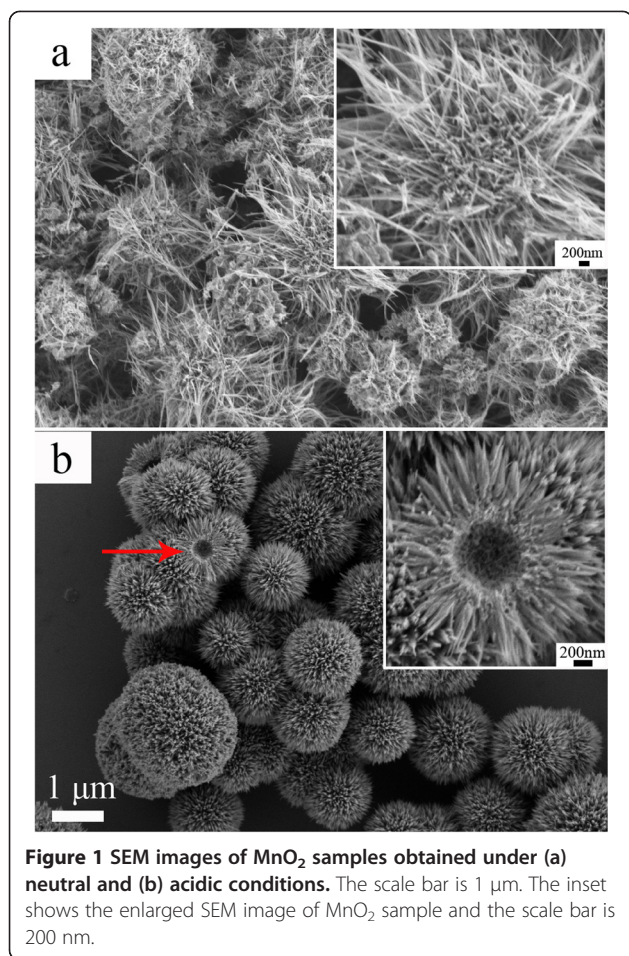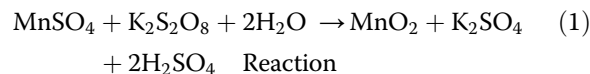
Figure 1 SEM images of MnO₂ samples obtained under (a) neutral and (b) acidic conditions. The scale bar is 1 μm. The inset shows the enlarged SEM image of MnO₂ sample and the scale bar is 200 nm.

MnO₂ micromaterial as caddice-clew-like MnO₂. As shown in Figure 1b, when sulfuric acid was added as morphology modulation agent, the MnO₂ micromaterial has a uniform sea-urchin-like shape with diameter of approximately 3 μm, which consists of several straight and radially grown nanorods with uniform length of about 1 μm. As indicated by the arrow in Figure 1b, the urchin-like MnO₂ microsphere has a hollow interior. Figure 2 illustrates the possible formation processes for the MnO₂ micromaterials. During the preparation of the MnO₂ micromaterials, the $K_2S_2O_8$ plays the role to oxidize the Mn^{2+} ion to MnO₂. Firstly, the tiny crystalline nuclei of MnO₂ are generated

from Mn^{2+} by the oxidation in the supersaturated solution and grow into nanoparticles. The nucleation process could be regarded as

$$MnSO_4 + K_2S_2O_8 + 2H_2O \rightarrow MnO_2 + K_2SO_4 \quad (1)$$
$$+ 2H_2SO_4 \quad \text{Reaction}$$

As can be seen in Reaction (1), the reaction rate is pH dependent. Therefore, sulfuric acid is added to decrease the reaction rate, and the morphology can be modulated. When no sulfuric acid is used, these primary nanoparticles form quickly (shown in Figure 2(a)). Then, the tiny nanoparticles spontaneously aggregate into long nanowires. With minimizing interfacial energies, the nanowires wrap with each other incompactly to form caddice-clew-shaped MnO₂ micromaterials. When sulfuric acid is added as morphology modulation agent, the nucleation process in Reaction (1) is suppressed. In this situation, it is not easy to form nanowires. Alternatively, short nanorods are formed (shown in Figure 2(b)). With minimizing interfacial energies, the nanorods self-assemble compactly to urchin morphology with a hollow interior. Thus, urchin-like MnO₂ micromaterials are prepared. Therefore, sulfuric acid plays a crucial role in the morphology evolution due to its control of the nucleation rate of MnO₂.

The XRD patterns of the MnO₂ micromaterials are shown in Figure 3. As shown, the two samples had similar crystallographic structure. The diffraction peaks which appeared at $2\theta = 12.7°$, 18.1°, 28.8°, 37.5°, 42.1°, 49.9°, 56.2°, and 60.3° matched well with the diffraction peaks of (110), (200),(310),(211),(301),(411),(600), and (521) crystal planes of α-MnO₂ standard data (JCPDS card PDF file no. 44-0141). Therefore, the two MnO₂ micromaterials prepared by hydrothermal method were both α-MnO₂, which was essential to evaluate the relationship between electrochemical performances and morphologies of MnO₂ crystals as anodes for lithium-ion battery. As calculated, the lattice parameters of caddice-clew-like MnO₂ are $a = 9.7875$ and $c = 2.8600$, which are highly identical to the standard values (JCPDS card PDF file no. 44-0141, $a = 9.7847$, $c = 2.863$). The cell volume of caddice-clew-like MnO₂ is 273.97 Å³ which is also highly identical to the standard values (274.1 Å³),while the lattice parameters of urchin-like MnO₂ are $a = 9.8084$ and $c = 2.8483$. According
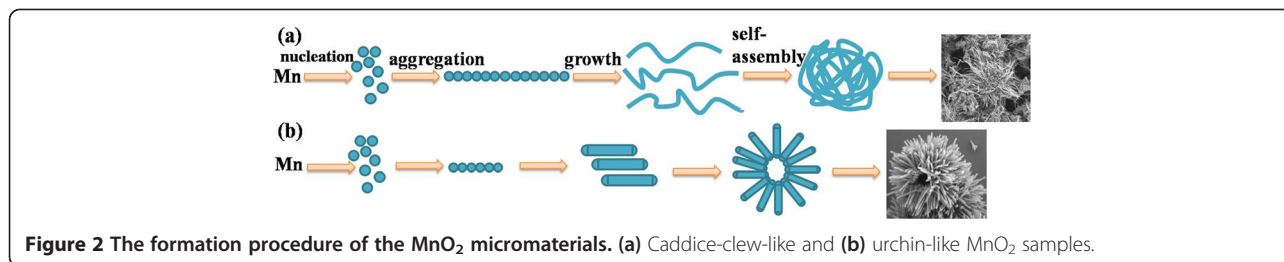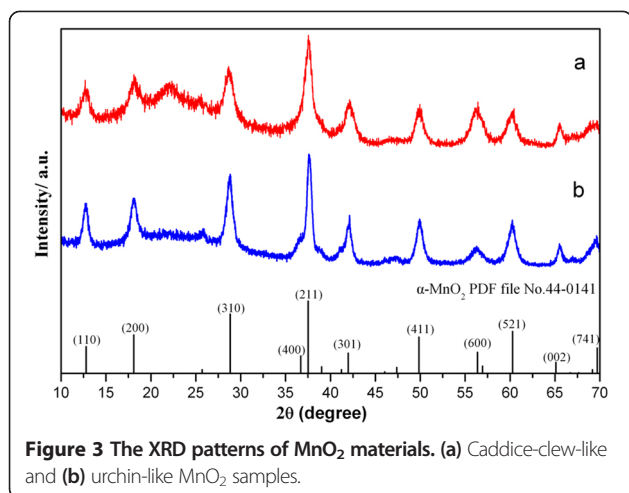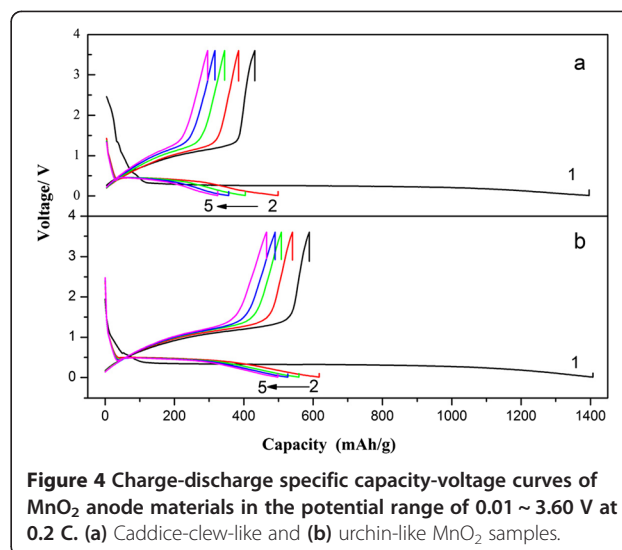

Figure 2 The formation procedure of the MnO₂ micromaterials. (a) Caddice-clew-like and **(b)** urchin-like MnO₂ samples.

Figure 3 The XRD patterns of MnO₂ materials. (a) Caddice-clew-like and **(b)** urchin-like MnO₂ samples.

Figure 4 Charge-discharge specific capacity-voltage curves of MnO₂ anode materials in the potential range of 0.01 ~ 3.60 V at 0.2 C. (a) Caddice-clew-like and **(b)** urchin-like MnO₂ samples.

to the standard values, the crystal cell expands in a and b directions and contracts in c direction. The cell volume of urchin-like MnO₂ is 274.02 Å³. The average size of the caddice-clew-like MnO₂ crystal grains is calculated to be 32 nm according to the Scherrer equation $D = K\lambda/\beta\cos\theta$ using the strongest diffraction peak of (211) [D is crystal grain size (nm), K is the Scherrer constant (0.89), λ is the X-ray wavelength (0.154056 nm) for Cu Kα, β is the full width at half maximum (FWHM) of the peak (211), and θ is the angle of diffraction peak],while the measured diameter of caddice-clew-like MnO₂ is 53 nm. The average size of the urchin-like MnO₂ crystal grains is calculated to be 51 nm according to the Scherrer equation. The measured diameter of the short nanorods on urchin-like MnO₂ is about 50 nm. As can be seen, the calculated crystallite size value of caddice-clew-like MnO₂ crystal is a little smaller than the measured value, but the calculated crystallite size value of urchin-like MnO₂ crystal is identical. Although the MnO₂ micromaterials are in micrometer scale, they are confirmed to assemble by nanomaterials. Consequently, although the two MnO₂ micromaterials are with identical crystal structure, they may have some difference in the electrochemical performance as the urchin-like MnO₂ has the expanded lattice parameters.

Electrochemical performance

Figure 4 presents the typical charge-discharge voltage curves of the anodes (compared to the full battery) constructed from MnO₂ micromaterials at 0.2 C rate in the voltage range of 0.01 to 3.60 V (vs. Li/Li⁺). For clarity, only selected cycles are shown. As shown, the two α-MnO₂ micromaterials both have high initial discharge specific capacity as approximately 1,400 mAh g⁻¹, while the theoretical discharge specific capacity is 1,232 mAh g⁻¹. The extra discharge specific capacities of the as-prepared MnO₂ micromaterials may result from the formation of solid electrolyte interface (SEI) layer which is known as a
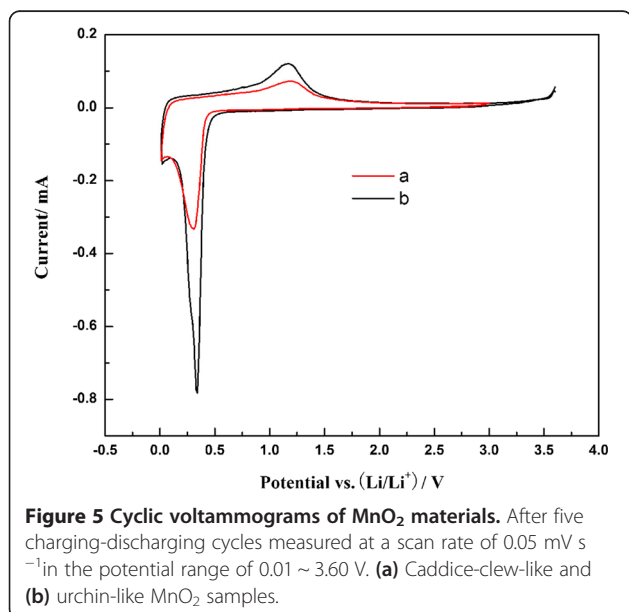
gel-like layer, containing ethylene oxide-based oligomers, LiF, Li₂CO₃, and lithium alkyl carbonate (ROCO₂Li), during the first discharging process [29]. The discharge specific capacities of the as-prepared MnO₂ micromaterials in the second cycle are 500 mAh g⁻¹(caddice-clew-like MnO₂) and 600 mAh g⁻¹ (urchin-like MnO₂), respectively. There is an attenuation compared to the initial discharge capacity. After the fifth cycling, the discharge specific capacities of the as-prepared MnO₂ micromaterials are 356 mAh g⁻¹ (caddice-clew-like MnO₂) and 465 mAh g⁻¹ (urchin-like MnO₂), respectively. In the repeated charge-discharge cycling, the discharge specific capacity eventually decays to about 250 mAh g⁻¹. Here, the large capacity loss may come from two facts: one is the capacity loss from the incomplete decomposition of SEI film, which happens in all 3d transition metal oxides including CuO, NiO, and Co₃O₄ [29]; the other one is capacity loss caused by the electrode pulverization and loss of inter-particle contact or the particle with copper foil collector due to large volume expansion/contraction during repeated charging-discharging processes and severe particle aggregation, which is common in all transition metal oxides [30]. In fact, both the MnO₂ micromaterials suffer from poor cycling stability of the discharge specific capacity. As usual, one effective way to mitigate the problem is to fabricate a hollow structure, as a hollow interior could provide extra free space for alleviating the structural strain and accommodating the large volume variation associated with repeated Li⁺ ion insertion/extraction processes, giving rise to improved cycling stability. However, the urchin-like MnO₂ in this research indeed has a hollow interior but poor cycling stability. So, another effective strategy to improve the cycling stability is the need for the as-prepared MnO₂ samples. For example, shell coating such as carbon coating, polypyrrole coating, and
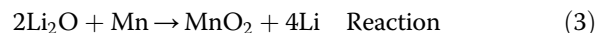
polyaniline coating is widely used to improve the cycling stability. Wan et al. prepared Fe_3O_4/porous carbon-multiwalled carbon nanotubes composite to promote cycle performance. Their excellent electrical properties can be attributed to the porous carbon framework structure, which provided space for the change in Fe_3O_4 volume during cycling and shortens the lithium ion diffusion distance [31]. Therefore, we are preparing polypyrrole coating MnO_2 micromaterials to enhance the cycling stability.

In addition, a discharge plateau with wide and flat shape appears in all the discharge voltage curves. Urchin-like MnO_2 micromaterial has a plateau at about 0.32 V from 120 to 1,100 mAh g^{-1} during the first discharging process and has a plateau from 50 to 360 mAh g^{-1} in the second cycling. The caddice-clew-like MnO_2 micromaterial has similar discharge plateau. The discharge plateau may bring stable discharge current to the battery prepared by MnO_2 micromaterials. According to the results of discharge specific capacity, urchin-like MnO_2 micromaterial was better than caddice-clew-like MnO_2 micromaterial.

The cyclic voltammogram curves were tested to further investigate the electrochemical performances of the MnO_2 micromaterials, as shown in Figure 5. In the CV curves, there is only a pair of redox peaks, indicating the one-step intercalation and deintercalation of lithium ion during the charging and discharging process. The reduction peak is at about 0.3 V, which corresponds well with flat discharge plateau in Figure 4. In this process, MnO_2 is transformed to Mn, and Li^+ is inserted into the anode to format Li_2O. The reaction is as follows:

$$MnO_2 + 4Li \rightarrow 2Li_2O + Mn \quad \text{Reaction} \quad (2)$$

Figure 5 Cyclic voltammograms of MnO_2 materials. After five charging-discharging cycles measured at a scan rate of 0.05 mV s^{-1} in the potential range of 0.01 ~ 3.60 V. **(a)** Caddice-clew-like and **(b)** urchin-like MnO_2 samples.

The oxidation peak is at about 1.18 V, corresponding to the charging process of the lithium-ion battery. During this process, Mn can facilitate the decomposition of Li_2O. The reaction of Li_2O with Mn was as follows:

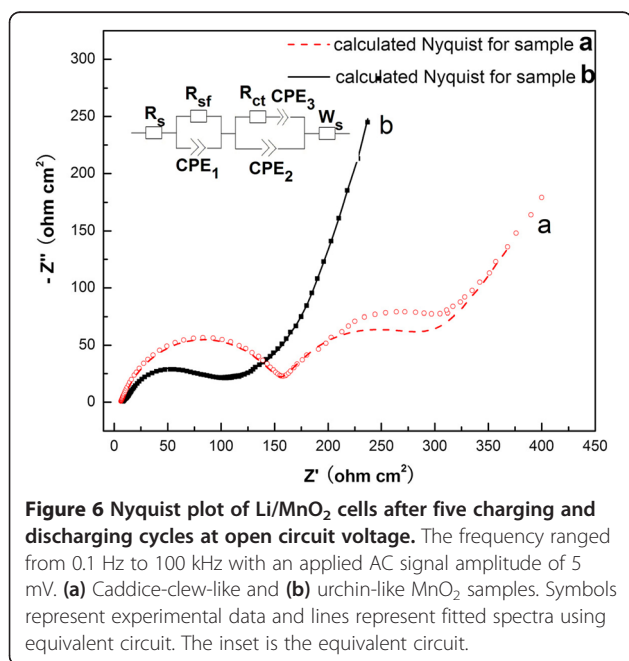$$2Li_2O + Mn \rightarrow MnO_2 + 4Li \quad \text{Reaction} \quad (3)$$

The current intensity of oxidation peak is much lower than that of reduction peak. The current intensity of reduction peak and oxidation peak for the urchin-like MnO_2 material is 0.7828 and 0.1202 mA mg^{-1}, respectively. The current intensity attenuation of oxidation peak indicates that Mn element could not completely convert to MnO_2 during the charging process. The shapes of the CV curves for the MnO_2 samples are similar, while urchin-like MnO_2 material has higher peak intensity. The current intensity of reduction peak and oxidation peak for the caddice-clew-like MnO_2 material is 0.3333 and 0.0712 mA mg^{-1}, respectively. The asymmetry cyclic voltammogram curves in Figure 5 indicate that the discharging/charging process is irreversible.

To exclude the influence of the MnO_2 micromaterial density on the electrode, we have normalized the CV curve in Figure 5. According to the results of galvanostatical charge-discharge experiments and CV tests, the urchin-like MnO_2 micromaterial is more superior than caddice-clew-like MnO_2 micromaterial. We presume the difference on electrochemical performance results from the morphology as both the MnO_2 micromaterials have identical crystalline phase. Theoretically, nanomaterials with incompact structure are beneficial to improve the transmission rate and transfer ability of lithium ion. However, the discharge cycling stability of caddice-clew-like MnO_2 micromaterial is poor. We guess the incompact structure may lead to easy electrode pulverization and loss of inter-particle contact during the repeated charging-discharging processes. A hollow structure which is another effective strategy to improve the cycling stability could provide extra free space for alleviating the structural strain and accommodating the large volume variation associated with repeated Li^+ insertion/extraction processes. So, the relatively better discharge cycling stability may result from the hollow structure. In addition, the surface of urchin-like MnO_2 is an arrangement of compact needle-like nanorods, which could improve the transmission rate and transfer ability of lithium ion. Therefore, the electrochemical performances of the MnO_2 micromaterials indeed have relationship on their morphologies. The results suggest that the urchin-like MnO_2 micromaterial is more promising for the anode of lithium-ion battery.

Compared to the literature [6], when MnO_2 materials were used for electrochemical supercapacitors, caddice-clew-like MnO_2 material had higher specific capacitance

of 120 F g^{-1} and lower charge-transfer resistance, while the specific capacitance of urchin-like MnO_2 material was about 48 F g^{-1}. Moreover, they found the unique capacitance of caddice-clew-like MnO_2 was mainly due to the incompact structure. Therefore, the relationship between electrochemical performance and morphology is different when MnO_2 material is used as electrochemical supercapacitor or as anode of lithium-ion battery. For the application on lithium-ion battery, urchin-like MnO_2 material is better.

In order to gain further understanding of the differences in the electrochemical performances, EIS testing was carried out. Figure 6 presents the EIS results for lithium cells after the fifth cycle at open circuit voltage. As shown in Figure 5(a), the impedance spectra of caddice-clew-like MnO_2 consist of two oblate semicircles in high-to-medium frequency region and an inclined line in low-frequency region, while the two semicircles of urchin-like MnO_2 are not easily distinguishable. The impedance spectra reflect several processes that take place in a series: Li migration through surface films, charge transfer, solid-state diffusion, and finally, accumulation of Li in the bulk of the active mass. An intercept at the Z_{real} axis in high-frequency region corresponds to the ohmic electrolyte resistance (R_s). The first semicircle in the high frequency ascribes to the Li-ion migration resistance (R_{sf}) through the SEI films. The second semicircle in the high-to-medium frequency ascribes to the charge transfer resistance (R_{ct}). The inclined line at low-frequency region represents the Warburg impedance (W_s), which is associated with lithium-ion diffusion in the active material [32,33].

The parameters of impedance spectra were simulated by ZSimpWin software, and the spectra had been fitted with an equivalent circuit shown in the inset of Figure 6. In the equivalent circuit of EIS, apart from the R_s, R_{sf}, R_{ct}, and W_s, the corresponding constant phase element (CPE) is used instead of pure capacitance due to the non-ideal nature of the electrode. The values of R_{sf} and R_{ct} calculated from the diameters of the high frequency and the high-to-medium frequency semicircles in the Nyquist plots for the electrodes are summarized in Table 1. The value of R_s for urchin-like MnO_2 is 7.12Ω, while the value of R_s for caddice-clew-like MnO_2 is 8.05Ω. Theoretically, the value of R_s for both Li/MnO_2 cells should be the same as for the same electrolyte used here. The slight difference may be caused by the tiny difference in the battery package pressure by manual operation or the tiny difference in the amount of electrolyte added to the Li/MnO_2 cells by manual operation. Considering the tiny difference in manual operation, the small difference of R_s is acceptable since the ohmic electrolyte resistances of the MnO_2 micromaterials are similar. The R_{sf} and R_{ct} of the urchin-like MnO_2 are much lower than that of the caddice-clew-like MnO_2. It proves that the Li-ion migration resistance through the SEI films and charge transfer resistance of the urchin-like MnO_2 are much lower than that of the caddice-clew-like MnO_2. Here, the influence of the tiny difference in the battery package pressure and the amount of electrolyte on the R_{sf} and R_{ct} can be neglected. So, the urchin-like morphology is more favorable for lithium ion diffusion and transfer, and the reaction of MnO_2 micromaterials with lithium ion is much easier.

Conclusions

In summary, two MnO_2 micromaterials with urchin-like and caddice-clew-like morphologies are prepared by hydrothermal method. Both the crystalline phases are α-MnO_2, which is essential to evaluate the relationship between electrochemical performances and morphologies of MnO_2 crystals as anodes for lithium-ion battery application. Both the as-prepared α-MnO_2 exhibit high initial specific capacity, but the discharge cycling stability is poor. Just in case of this research, the urchin-like MnO_2 material has better electrochemical performance. The results suggest that different morphologies indeed have

Figure 6 Nyquist plot of Li/MnO$_2$ cells after five charging and discharging cycles at open circuit voltage. The frequency ranged from 0.1 Hz to 100 kHz with an applied AC signal amplitude of 5 mV. **(a)** Caddice-clew-like and **(b)** urchin-like MnO_2 samples. Symbols represent experimental data and lines represent fitted spectra using equivalent circuit. The inset is the equivalent circuit.

Table 1 R_s, R_{sf}, and R_{ct} calculated from Nyquist plots for the MnO_2 materials

	R_s (Ω cm^2)	R_{sf} (Ω cm^2)	R_{ct} (Ω cm^2)
a	8.05	121.40	146.90
b	7.12	94.66	43.64

a, caddice-clew-like MnO_2 sample; b, urchin-like MnO_2 sample.

influence on electrochemical performances of MnO_2 micromaterials in the application of lithium-ion battery. This study also gives us advice to make shell coating on the as-prepared MnO_2 micromaterials to improve the cycling stability.

Competing interests

The authors declare that they have no competing interests.

Authors' contributions

The experiments and characterization presented in this work were carried out by LF, ZX, HZ, and YB. The experiments were designed by LF. The results of the experiments were discussed by LF, JG, CS, and XC. All authors read and approved the final manuscript.

Author details

[1]Engineering Research Center of Biopolymer Functional Materials of Yunnan, Yunnan Minzu University, Kunming 650500, China. [2]Key Laboratory of Chemistry in Ethnic Medicinal Resources, State Ethnic Affairs Commission & Ministry of Education, Yunnan Minzu University, Kunming 650500, China. [3]College of Civil Engineering, Kunming University of Science & Technology, Kunming 650500, China.

References

1. Sui N, Duan Y, Jiao X, Chen D: **Large-scale preparation and catalytic properties of one-dimensional MnO₂ nanostructures.** *J Phys Chem C* 2009, **113**:8560–8565.
2. Zhang W, Zeng C, Kong M, Pan Y, Yang Z: **Water-evaporation-induced self-assembly of α-MnO₂ hierarchical hollow nanospheres and their applications in ammonia gas sensing.** *Sens Actuators B* 2012, **162**:292–299.
3. Fei J, Cu Y, Yan X, Qi W, Yang Y, Wang K, He Q, Li J: **Controlled preparation of MnO₂ hierarchical hollow nanostructures and their application in water treatment.** *Adv Mater* 2008, **20**:452–456.
4. Cao J, Mao Q, Shi L, Qian Y: **Fabrication of g-MnO₂/α-MnO₂ hollow core/shell structures and their application to water treatment.** *J Mater Chem* 2011, **21**:16210–16215.
5. Wei W, Cui X, Chen W, Ivey DG: **Manganese oxide-based materials as electrochemical supercapacitor electrodes.** *Chem Soc Rev* 2011, **40**:1697–1721.
6. Yu P, Zhang X, Wang D, Wang L, Ma Y: **Shape-controlled synthesis of 3D hierarchical MnO₂ nanostructures for electrochemical supercapacitors.** *Cryst Growth Des* 2009, **9**:528–533.
7. Subramanian V, Zhu H, Wei B: **Nanostructured MnO₂: hydrothermal synthesis and electrochemical properties as a supercapacitor electrode material.** *J Power Sources* 2006, **159**:361–364.
8. Jiang R, Huang T, Liu J, Zhuang J, Yu A: **A novel method to prepare nanostructured manganese dioxide and its electrochemical properties as a supercapacitor electrode.** *Electrochim Acta* 2009, **54**:3047–3052.
9. Subramanian V, Zhu H, Vajtai R, Ajayan PM, Wei B: **Hydrothermal synthesis and pseudocapacitance properties of MnO₂ nanostructures.** *J Phys Chem B* 2005, **109**:20207–20214.
10. Xu M, Kong L, Zhou W, Li H: **Hydrothermal synthesis and pseudocapacitance properties of γ-MnO₂ hollow spheres and hollow urchins.** *J Phys Chem C* 2007, **111**:19141–19147.
11. Li Z, Ding Y, Xiong Y, Xie Y: **Rational growth of various γ-MnO₂hierarchical structures and α-MnO₂ nanorods via a homogeneous catalytic route.** *Cryst Growth Des* 2005, **5**:1953–1958.
12. Wang X, Li Y: **Rational synthesis of α-MnO₂ single-crystal nanorods.** *Chem Commun* 2002:764–765.
13. Duan X, Yang J, Gao H, Ma J, Jiao L, Zheng W: **Controllable hydrothermal synthesis of manganese dioxide nanostructures: shape evolution, growth mechanism and electrochemical properties.** *Cryst Eng Comm* 2012, **14**:4196–4204.
14. Li WN, Yuan J, Shen XF, Gomez-Mower S, Xu LP, Sithambaram S, Aindow M, Suib SL: **Hydrothermal synthesis of structure- and shape-controlled manganese oxide octahedral molecular sieve nanomaterials.** *Adv Funct Mater* 2006, **16**:1247–1253.
15. Li L, Nan C, Lu J, Peng Q, Li Y: **α-MnO₂ nanotubes: high surface area and enhanced lithium battery properties.** *Chem Commun* 2012, **48**:6945–6947.
16. Song XC, Zhao Y, Zheng YF: **Synthesis of MnO₂ nanostructures with sea urchin shapes by a sodium dodecyl sulfate-assisted hydrothermal process.** *Cryst Growth Des* 2007, **7**:159–162.
17. Portehault D, Cassaignon S, Baudrin E, Jolivet JP: **Twinning driven growth of manganese oxide hollow cones through self-assembly of nanorods in water.** *Cryst Growth Des* 2009, **9**:2562–2565.
18. Poizot P, Laruelle S, Grugeon S, Dupont L, Tarascon JM: **Nano-sized transition-metal oxides as negative-electrode materials for lithium-ion batteries.** *Nature* 2000, **407**:496–499.
19. Kim DK, Muralidharan P, Lee HW, Ruffo R, Yang Y, Chan CK, Peng H, Huggins RA, Cui Y: **Spinel LiMn₂O₄ nanorods as lithium ion battery cathodes.** *Nano Lett* 2008, **8**:3948–3952.
20. Luo J, Cheng L, Xia Y: **LiMn₂O₄ hollow nanosphere electrode material with excellent cycling reversibility and rate capability.** *Electrochem Commun* 2007, **9**:1404–1409.
21. Cheng F, Zhao J, Song W, Li C, Ma H, Chen J, Shen P: **Facile controlled synthesis of MnO₂ nanostructures of novel shapes and their application in batteries.** *Inorg Chem* 2006, **45**:2038–2044.
22. Zhao J, Tao Z, Liang J, Chen J: **Facile synthesis of nanoporous γ-MnO₂ structures and their application in rechargeable Li-ion batteries.** *Cryst Growth Des* 2008, **8**:2799–2805.
23. Wu HB, Chen JS, Hng HH, Lou XWD: **Nanostructured metal oxide-based materials as advanced anodes for lithium-ion batteries.** *Nanoscale* 2012, **4**:2526–2542.
24. Zhang WM, Wu XL, Hu JS, Guo YG, Wan LJ: **Carbon coated Fe₃O₄ nanospindles as a superior anode material for lithium-ion batteries.** *Adv Funct Mater* 2008, **18**:3941–3946.
25. Barreca D, Cruz-Yusta M, Gasparotto A, Maccato C, Morales J, Pozza A, Sada C, Sánchez L, Tondello E: **Cobalt oxide nanomaterials by vapor-phase synthesis for fast and reversible lithium storage.** *J Phys Chem C* 2010, **114**:10054–10060.
26. Barreca D, Carraro G, Gasparotto A, Maccato C, Cruz-Yusta M, Gómez-Camer JL, Morales J, Sada C, Sánchez L: **On the performances of CuₓO-TiO₂(x = 1, 2) nanomaterials as innovative anodes for thin film lithium batteries.** *ACS Appl Mater Interfaces* 2012, **4**:3610–3619.
27. Zhang L, Wu HB, Madhavi S, Hng HH, Lou XW: **Formation of Fe₂O₃ microboxes with hierarchical shell structures from metal-organic frameworks and their lithium storage properties.** *J Am Chem Soc* 2012, **134**:17388–17391.
28. Wang C, Zhou Y, Ge M, Xu X, Zhang Z, Jiang JZ: **Large-scale synthesis of SnO₂ nanosheets with high lithium storage capacity.** *J Am Chem Soc* 2012, **132**:46–47.
29. Xiang JY, Tu JP, Zhang L, Zhou Y, Wang XL, Shi SJ: **Self-assembled synthesis of hierarchical nanostructured CuO with various morphologies and their application as anodes for lithium ion batteries.** *J Power Sources* 2010, **195**:313–319.
30. Chen J: **Recent progress in advanced materials for lithium ion batteries.** *Materials* 2013, **6**:156–183.
31. Wan W, Wang C, Zhang W, Chen J, Zhou H, Zhang X: **Superior performance of nanoscaled Fe₃O₄ as anode material promoted by mosaicking into porous carbon framework.** *Funct Mater Lett* 2014, **7**:1450005–4.

32. Gao XW, Feng CQ, Chou SL, Wang JZ, Sun JZ, Forsyth M, MacFarlane DR, Liu HK: LiNi$_{0.5}$Mn$_{1.5}$O$_4$ spinel cathode using room temperature ionic liquid as electrolyte. *Electrochim Acta* 2013, **101**:151–157.
33. Feng L, Xuan Z, Bai Y, Zhao H, Li L, Chen Y, Yang X, Su C, Guo J, Chen X: Preparation of octahedral CuO micro/nanocrystals and electrochemical performance as anode for lithium-ion battery. *J Alloys Compd* 2014, **600**:162–167.